

# Data efficient protein backmapping with backbone-to-side chain transformers

Shriram Chennakesavalu and Grant M. Rotskoff

November 2023

## Abstract

Excitement at the prospect of using data-driven generative models to sample configurational ensembles of biomolecular systems stems from the extraordinary success of these models on a diverse set of high-dimensional sampling tasks. Unlike image generation or even the closely related problem of protein structure prediction, there are not currently data sources with sufficient breadth to parameterize generative models for conformational ensembles. To enable discovery, a fundamentally different approach to building generative models is required: models should be able to propose rare, albeit physical, conformations that may not arise in even the largest data sets. Here we introduce a modular strategy to generate conformations based on “backmapping” from a fixed protein backbone that 1) maintains conformational diversity of the side chains and 2) couples the side chain fluctuations using global information about the protein conformation. Our model combines simple statistical models of side chain conformations based on rotamer libraries with the now ubiquitous transformer architecture to sample with atomistic accuracy. Together, these ingredients provide a strategy for rapid data acquisition and hence a crucial ingredient for scalable physical simulation with generative neural networks.

Generative models offer an appealing route to efficiently sample biomolecular conformational ensembles [1, 2, 3]. The high-dimensional, metastable probability distributions characteristic of thermal ensembles of large biomolecules are notoriously difficult to sample [4], requiring sophisticated importance sampling techniques [5] and high-performance computing [6]. While generative models may reduce the expense of exploring conformational space, there are not yet scalable methods for training these models. At present, the most powerful techniques for generative modeling have shown promise primarily on tasks where massive data sets are readily available [7, 8, 9]. For molecular systems, data is limited by the low spatial resolution of single-molecule measurements and the aforementioned cost of molecular dynamics (MD) simulation. In large-scale databases of three-dimensional protein structures, like the Protein Data Bank, rare but important transition states and metastable configurations are entirely absent. Building generative models that do not depend on task-specific data and that can be deployed on new biomolecular systems with little or no molecule-specific adaptation remains a defining challenge for this emerging field.

To construct models that do not require task-specific data, there are two dominant strategies: First, one can use data from a closely related task that is inexpensive to acquire and carry out transfer learning. While this approach is appealing, designing a transfer learning strategy that does not over-constrain the model and result in negative transfer can be challenging [10, 11]. Secondly, building a model that incorporates strong physical inductive biases in the form of constraints or preconditioners can improve generalization by ensuring that generated samples respect the imposed constraints [3, 12]. At the same time, imposing these restrictions may impact the trainability and expressiveness of the model in ways that are unproductive [13]. Strategies for combining these strategies to build truly transferable generative models is an area of ongoing research.

In parallel to the rapid developments of state-of-the-art generative models for image generation, an improved understanding of how to use normalizing flows [14, 15] for variational inference tasks has begun to emerge [16]. Normalizing flows are deterministic diffeomorphisms that transform samples from a tractable probability distribution, like a Gaussian, to a given target distribution. Because the likelihoods can be computed explicitly and efficiently for some architectures [17, 18], it is possible to train these models *without data*, using a maximum likelihood objective. Unfortunately, mode collapse, a phenomenon in which all the probability mass of the generated distribution collapses on a single mode, appears to be a fundamental issue

with this *data-free* training approach for metastable distributions. Our previous work [2] showed that combining physics-based coarse-grained models with an invertible backmapping strategy mitigates mode collapse and enables a sampling strategy that is amenable to exact reweighting. However, the procedure we used for backmapping coarse-grained structures, while statistically controlled in the sense that it ensures Boltzmann statistics, is not “task-independent,” and the framework we employed was limited by the requirement of atomistic configurational data of the target molecule.

Throughout this work, we focus on the problem of reconstructing an atomic resolution protein structure from only information about its backbone coordinates. Understanding and analyzing the side chain conformations available to different residue types, as well as their dependence on the backbone configuration, is an old problem. Early work [19] established that the number of rotameric states available to the side chains of biological amino acids was finite, which has since prompted statistical investigations into the sequence dependence of these side chain rotameric state [20, 21]. Backmapping protein structures from a coarse-grained configuration, often the backbone, bears a statistical resemblance to Levinthal’s famous “paradox” [22] which is resolved simply with the recognition that the strong correlations—arising due to the potential energy—among rotamers limits the number of thermodynamically accessible states. So, while the many-body energetic interactions among the atoms of a protein constrain its structure, a naive attempt to sample a configuration by independently sampling rotamers along a backbone will fail. Indeed, direct investigations of the correlations between side chains in a protein indicate that the information propagates on a scale comparable to the extent of the protein itself [23, 24, 25].

Due to the tractable structure of rotamer distributions, several groups have pursued efforts to systematically enumerate the available states [26, 27]. Furthermore, these libraries have subsequently been deployed to capture the sequence dependence of side chains using relaxation algorithms [28, 29, 30]. Recently, this topic has been revisited in the context of more expressive probabilistic models built with deep neural networks [31, 2, 32, 33]. However, in large part, these efforts have not sought to add physically meaningful thermal stochastic fluctuations.

In this work, we aim to build samplers that demonstrate high levels of agreement for correlated side chain configurations with Boltzmann distributed configurations from atomistic MD. We do so by exploiting the observation that rotamer libraries can easily be modeled at single side-chain resolution with a Gaussian mixture model, as demonstrated below. The most challenging aspect of backmapping is then reduced to learning the coupling among these simple probabilistic models. This problem—given a backbone sequence, generate a sequence of side chains consistent with that backbone conformation—is very naturally suited to sequence-to-sequence models capable of capturing long-range correlations, such as transformers [34]. We demonstrate that learning a many-body coupling among side chain conformations from rotamer libraries with a transformer yields backmapped configurations in excellent agreement with atomistic simulations, despite never training on data from the target protein. This level of generalization lends itself to rapid enumeration of conformational states that may only interconvert on timescales inaccessible to MD.

## 1 Related Work

**Backmapping coarse-grained representations** A number of works have explored backmapping from a coarse-grained representation of a molecular system to atomistic resolution. Deterministic algorithms that construct an atomistic configuration that avoids steric clashes have been proposed for both proteins [28, 30] and DNA [35]. Of course, because these algorithms are deterministic, they do not recover the entropy lost when coarse-graining. More recently, several stochastic approaches based on generative neural networks have been proposed. For example, Stieffenhofer et al. [31] trained generative adversarial networks to reconstruct protein structural ensembles. Similar tasks have been pursued with different architectures [32, 33]. Our previous work seeks not only to add stochasticity to this task but to ensure that the sampled distribution can be reweighted to ensure Boltzmann statistics: we carry this out by training normalizing flows that conditionally sample rotamers given a backbone conformation [2]. However, unlike Refs. [32, 33], the models developed in Ref. [2] trained for individual proteins and are not general purpose.

**Monte Carlo with generative models** A number of recent works have sought to improve sampling using generative machine learning. For Markov Chain Monte Carlo, [1] used normalizing flows that were

optimized to sample Boltzmann distributions, though this problem requires task-specific data [36] and is difficult to scale to large systems. Alternative approaches using distinct strategies for Monte Carlo [37, 38] have not found applications in physical systems due to complex training objectives. Generative models have also been used to refine data and improve accuracy [39].

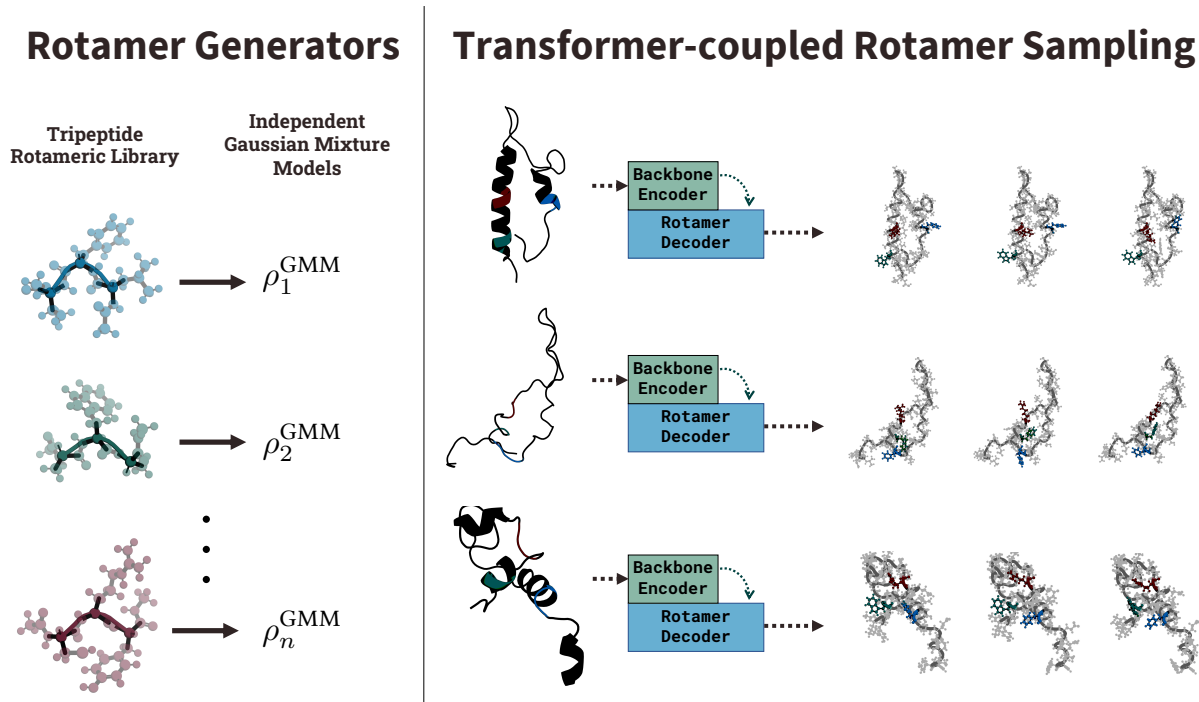


Figure 1: A schematic overview of backmapping procedure. First, for a given protein, a rotameric library of all unique tripeptide fragments is generated via long MD simulations in explicit solvent. Next, for each of these tripeptides, a unique and independent rotamer generator, represented by a Gaussian mixture model, is trained. Finally, these independent rotamer generators are coupled via a transformer, and for a given backbone structure, the transformer generates an ensemble of side chain rotamer states. Select generated side chains are colored and correspond to the respective colored tripeptides depicted on the left.

## 2 Independent Rotamer Generators

It has long been observed the protein side chains occupy a small number of rotameric states [19]. These observations have led to the curation of so-called rotamer libraries which tabulate metastable conformations of certain side chain atoms, usually by recording their  $\chi$  dihedral angles [40, 41]. The distribution of allowed  $\chi$  dihedral angles is dependent on the backbone conformation and on adjacent side chains, and this has led to rotamer libraries that incorporate varying degrees of information about the backbone, primary sequence, secondary structure, and protein type [21, 42, 20, 26]. The information from these rotamer libraries has been exploited in many different settings, including protein structure prediction [43], protein-ligand docking [44, 45, 46], and backmapping from coarse-grained simulations [30].

Recent work by Dicks and Wales constructed a backbone-independent, sequence-dependent rotamer library for all possible tripeptides consisting of naturally occurring amino acids [27]. Still, many rotamer libraries, including [27] only record a collection of metastable states corresponding to free-energy minima. Furthermore, these calculations are performed in implicit solvent. While practically useful in many settings, this information does not capture the full rotameric entropy of a side chain, which is crucial for statistically meaningful reconstruction of the side chain.

Inspired by the tripeptide simulations of [27], we sought to construct our own rotamer library that could capture the full rotameric entropy in a sequence-dependent fashion. To do so, we ran extensive molecular

dynamics simulations of tripeptides in explicit solvent, and for every saved frame, recorded the appropriate internal coordinates for each atom in the side chain (see Appendix A.1 for full details). Given the relatively small size of these tripeptide systems, these simulations offer an appealing route for carrying out data acquisition for larger protein systems. A protein of interest can be fragmented into individual tripeptides, and through MD simulations, these tripeptide simulations can produce large amounts of data about rotamer states for individual side chains of the protein, avoiding the scaling bottlenecks of MD.

Many state-of-the-art generative models perform best in the large data limit, meaning that if we can leverage the training data of the generated library, we can use this data to build accurate generative models. For a given tripeptide, we train a model on side chain dihedral angles sampled during an MD simulation and use that model to then carry out rotamer sampling. Given that the number of dihedrals for any single side chain is relatively small [19] and that the distribution of the  $\chi$  dihedrals generally has well-separated modes each of which appears to be approximately Gaussian (see Figure 7), we use a Gaussian mixture model (GMM) to represent our individual rotamer generators. The form of the distribution for each residue is

$$\rho^{\text{GMM}} = \sum_{i=1}^K \phi_i \mathcal{N}(\mu_i, \Sigma_i) \quad (1)$$

where  $K$  depends on the residue type and is chosen by inspection, though we note that this could also be done with a metric like the Bayesian information criterion.

Using GMMs offers two advantages. First, training a GMM on with data from the generated rotamer library is computationally inexpensive taking only a few CPU minutes per residue. Generative models based on deep neural networks such as normalizing flows or diffusion models can require hundreds of GPU-hours [47]. Second, each Gaussian component of the GMM can be loosely interpreted as a rotameric state of a particular side chain. While this interpretation is more tenuous for certain atoms in side chains like serine and threonine (see Figure 7), where rotamer modes may be less Gaussian-like, it holds for most atoms across all side chains. In sum, the GMM-based rotamer generators enable rapid sampling of rotamer states for a given residue, providing a means of carrying out backmapping from a backbone configuration.

### 3 Transforming backbone states to side chain distributions

A scheme that employs independent sampling of residue-wise rotamer generators will face a computational bottleneck; most generated structures will be statistically unlikely due to unfavorable energetics. Moreover, for large proteins, there are strong correlations among side chain rotamers, even for residues that are spatially and sequentially distant [25]. This bottleneck can be avoided by coupling the independent generators, though this requires both learning correlations between side chains and conditioning on the backbone structure. A scheme that couples rotamer generators—which individually are faithful to the underlying statistics of the side chain—amounts to enforcing a strong physical prior on the backmapping process.

While they are not determinative of a single backbone conformation, the  $\phi$  and  $\psi$  backbone dihedral angles provide information about secondary structure motifs [48] and importantly constrain both the backbone and side chain dihedral angles [42]. Parameterizing the backbone by a sequence of  $\phi$  and  $\psi$  angles, we seek to generate a *sequence* of rotameric states conditioned on the *sequence* of backbone conformations. This requires a sequence-to-sequence transformation that captures both short-ranged and long-ranged correlations among components in the sequence. The multi-head self-attention mechanism [34], foundational to many state-of-the-art seq2seq approaches, is well-suited to this task.

The architecture we use builds on the standard encoder-decoder-based transformer architecture [34], where the backbone encoder block inputs a backbone sequence and the rotamer decoder block autoregressively generates the rotamer state. Our encoder and decoder blocks both use a multi-head self-attention mechanism with 8 heads, 6 layers, and an embedding dimension of 256. The generation process begins with a continuous backbone tokenization scheme in which the backbone coordinates  $\mathbf{x}^{(n)} \in \mathbb{R}^{3n}$  are featurized as

$$(\mathbf{x}_1, \dots, \mathbf{x}_n) \mapsto \begin{bmatrix} \sin(\phi_1) & \sin(\phi_2) & \cdots & \sin(\phi_m) \\ \cos(\phi_1) & \cos(\phi_2) & \cdots & \cos(\phi_m) \\ \sin(\psi_1) & \sin(\psi_2) & \cdots & \sin(\psi_m) \\ \cos(\psi_1) & \cos(\psi_2) & \cdots & \cos(\psi_m) \end{bmatrix}. \quad (2)$$

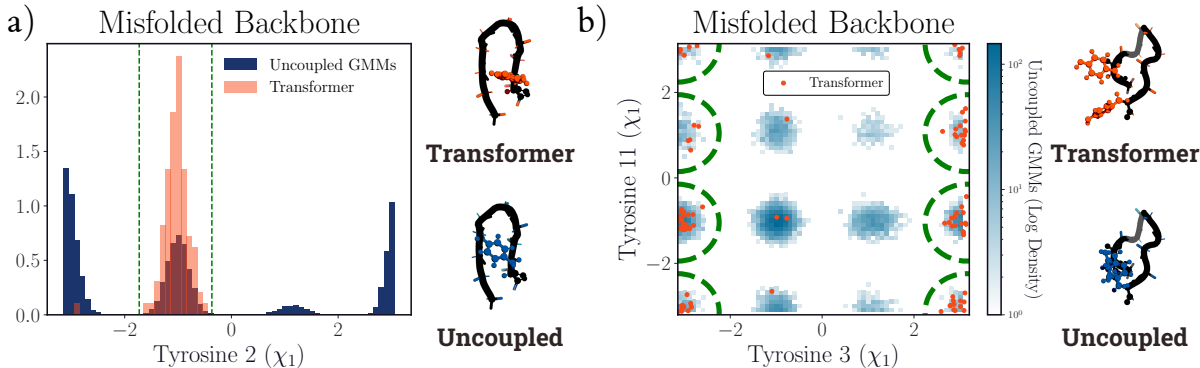


Figure 2: Backmapping generates physically meaningful rotamer states of terminal bulky side chains for a representative misfolded backbone. While all side chains are backmapped, only select residues are shown for clarity. a) Uncoupled sampling of Tyr2 results in samples with backbone clashes, while transformer-coupled sampling restricts sampling to physically allowed mode delineated in green (centered at  $-\frac{\pi}{3}$ ). b) Transformer-coupled sampling accurately captures correlations between Tyr3 and Tyr11 and restricts sampling to allowed modes delineated in green, while uncoupled sampling results in samples with steric clashes.

We use the featurization in Eq. 2 to avoid ambiguities with the periodicity of the dihedral angle coordinates. We also incorporate a categorical backbone tokenization scheme that embeds the residue identity using a standard lookup-table-based learnable embedding layer. The continuous and categorical embeddings are concatenated before being passed through a standard sinusoidal positional encoding layer. This embedded backbone sequence is then passed into the encoder block of the transformer.

Relying on the interpretation that each Gaussian component of a rotamer generator corresponds to a particular rotamer state, we autoregressively output a sequence of Gaussian components via the rotamer decoder block. That is, we want the transformer to generate a sequence of side chain rotamer states that are statistically likely under a thermal Boltzmann distribution. Upon determining a sequence of Gaussian components, we can then straightforwardly generate the coordinates of all side chain atoms by sampling internal coordinates from the selected Gaussian components (see Appendix A.2 for further details). For the systems we study here, the training data is collected by sampling rotamer generators independently, carrying out a short relaxation step, and retaining all configurations below a fixed cutoff energy. We note that this initial data collection is meant primarily to provide a test of the approach; in a more general setting, we envision relying on additional and diverse protein structural and trajectory data (see Section 5).

## 4 Results

### 4.1 Chignolin

The miniprotein Chignolin is a fast-folding, ten-residue protein. At equilibrium, Chignolin fluctuates between three metastable states: an unfolded state, a folded state, and a misfolded state [6, 49]. Here, we consider the CLN205 variant of Chignolin which is known to adopt a  $\beta$ -hairpin structure in its folded state [50]. The mechanisms of Chignolin folding are well-studied and occur first via a “hydrophobic collapse,” followed by further rearrangements [51]. Here, we assume that we have access to a collection of coarse-grained backbone configurations that we are interested in backmapping from, which we collect by coarse-graining atomistic configurations from a long all-atom MD simulation [49].

Chignolin can be split into 8 unique tripeptides, and for each of these tripeptides, we carry out long MD simulations in explicit solvent. To simplify the generation process, we work with internal coordinates, namely bond lengths, bond angles, and dihedral angles, and for each side chain atom, we record the appropriate set of internal coordinates in our generated rotamer library. For each residue, using a standard Expectation-Maximization (EM) algorithm, we train two Gaussian mixture models (GMMs): a GMM trained on the

## van der Waals Interactions (Misfolded Configurations)

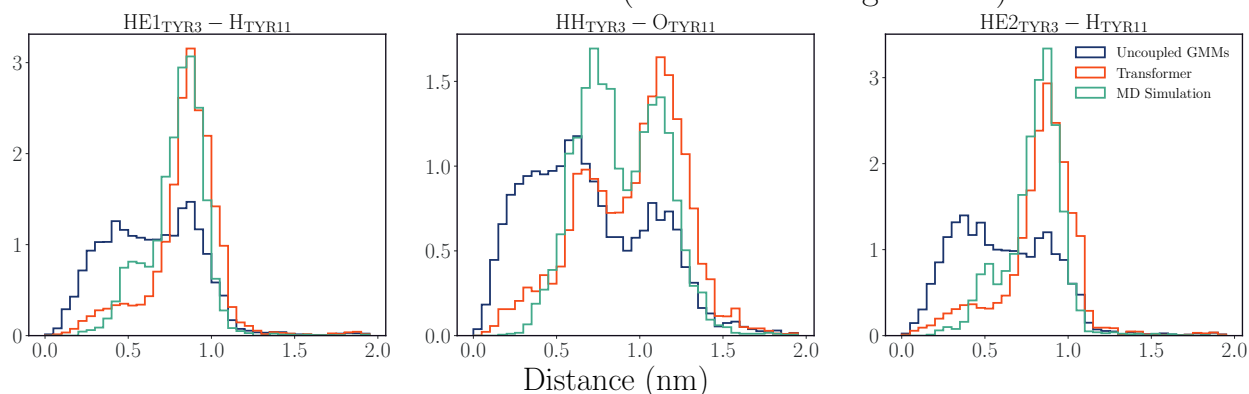


Figure 3: Backmapping captures van der Waals interactions between nearby non-bonded atoms for an ensemble of misfolded backbones. For select pairs of atoms highlighted, uncoupled sampling results in samples with high-energy interatomic distances; with transformer-coupled sampling, unphysical distances are greatly minimized, and importantly, are in strong agreement with distances observed during long MD simulations.

joint distribution of bond lengths and bond angles and a second GMM trained on the dihedral angles (See Appendix A.3 for further details). These rotamer generators can then be used to iteratively reconstruct an entire side chain.

A backmapping strategy that can approximately sample the true underlying conditional Boltzmann distribution of course requires a way to couple these independent rotamer generators, which we do using a transformer (see Section 3, Appendix B for further details). With Chignolin, for each of the 50000 backbone configurations, we generate 10000 possible rotamer states by independently sampling all rotamer generators, relax those structures using a short MD step, and select all structures with energies below a threshold (see Appendix C). We emphasize that this dataset does *not* consist of Boltzmann-distributed samples, but it does consist of configurations that individually have a reasonable probability mass within the Boltzmann distribution. Finally, we use an 80/10/10 train/validation/test-set split, where we carry out the split across backbone configurations, so no single backbone configuration is present in two or more of these split datasets. We train the transformer using a standard cross-entropy loss, select the best-performing network on the validation set, and carry out all analyses below on the test set.

### Backmapping of terminal side chains involved in hydrophobic collapse

The terminal bulky residues of Chignolin are primarily implicated in hydrophobic collapse [51], and first, we investigate our ability to backmap these residues. The misfolded state of Chignolin is characterized by the N-terminal end of the protein bending towards the interior of the hairpin. Practically, this results in an interior that is more tightly packed than the folded or unfolded state. As an initial test, we consider the distribution of  $\chi_1$  dihedral angles for the first tyrosine residue (Tyr2) in the sequence on a representative misfolded backbone. The  $\chi_1$  dihedral angle influences the position of the  $\gamma$ -Carbon and can be intuited as the overall orientation of the residue relative to the backbone, with downstream dihedral angles  $\chi_{2...K}$  influencing the local structure of the Tyrosine ring.

In Figure 4, we plot the distribution of  $\chi_1$  generated via uncoupled rotamer generators and compare with  $\chi_1$  generated from transformer-coupled rotamer sampling. First, we note that during sampling from the independent rotamer generators, we sample from the three different rotamer states (centered at  $-\frac{\pi}{3}$ ,  $\frac{\pi}{3}$ , and  $\pi$ ) in a proportion commensurate with that observed during the respective tripeptide simulation. For the representative misfolded backbone, the rotamer state centered at  $\pi$  will result in Tyr2 sterically clashing with the backbone, while the state centered at  $\pi/3$  is a statistically likely higher energy rotamer state. With transformer-informed sampling, sampling is limited to a statistically likely rotamer state.

Next, we consider the correlations between Tyrosine 3 and Tyrosine 11, two additional bulky side chains

## Hydrogen Bonds (Misfolded Configurations)

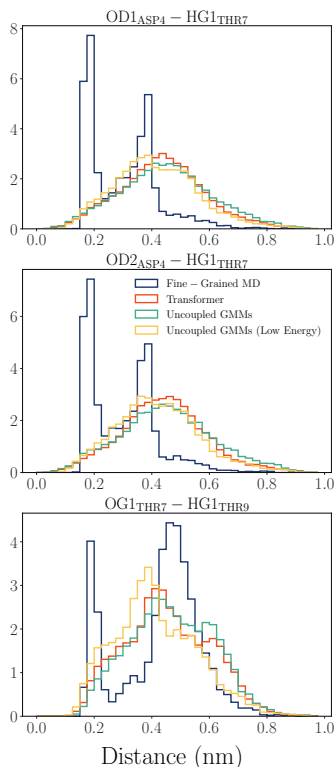


Figure 4: Backmapping does not fully capture hydrogen bonds for an ensemble of misfolded backbones. For atoms that engage in hydrogen bonds, transformer-coupled sampling does not in interatomic distances in agreement with long MD simulation. This is primarily a limit of the data curation strategy as evidenced by the agreement with relaxed, low energy samples (yellow). Strategies for overcoming this are outlined in Section 5.

also involved in hydrophobic collapse. While spatially proximal in a collapsed state, these residues are sequentially distant, providing an important test for whether the transformer-coupled sampling captures long-range correlations in the backbone sequence. In Figure 4, we plot the distribution of the respective distribution of  $\chi_1$  dihedral angles for the two residues. With uncoupled sampling, all 9 rotamer states are sampled to differing proportions; however, with transformer-coupled sampling, most of the samples are within the 3 energetically favorable modes—delineated in green—with only a few samples in modes that are statistically unlikely either as a result of a side-chain-backbone clash or a side-chain-side-chain clash.

Finally, we plot the distribution of all rotamer states across all backbones in Figure C.1. We observe that as the hairpin interior becomes more obstructed, the rotamer entropy decreases; more states become disallowed. This is a trend that we also observe in the MD simulation [49]. We note that the MD simulation is not exhaustive and does not fully sample all rotamer states and so only provides qualitative insight into the effect of different backbone metastable states on the rotamer distribution.

### Analysis of non-bonded interactions

The backmapping strategy we employ here relies on strong implicit physical priors about allowed bond lengths, bond angles, and dihedrals through individual rotamer generators. However, it does not incorporate priors about non-bonded distances. To determine the efficacy of our approach, we examine select non-bonded interactions of Chignolin. First, we consider pairs of side chain atoms that have only non-bonded van der Waals and electrostatic interactions. We plot the distribution of distances between three of these pairs in Figure 3, which consists of various atom pairs between Tyrosine 3 and Tyrosine 11. We observe that

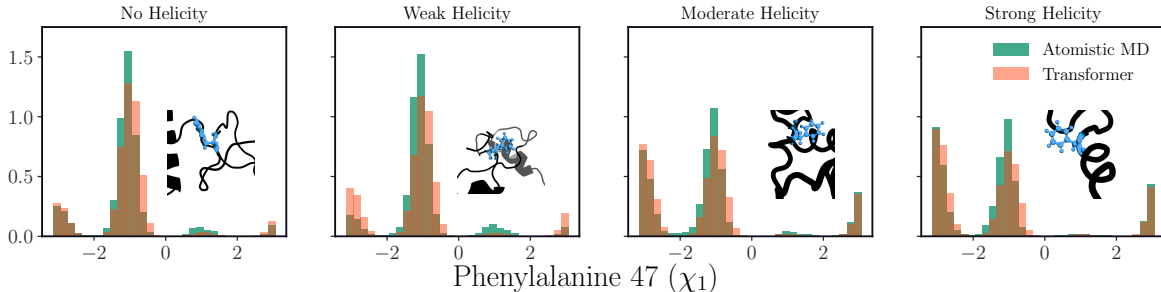


Figure 5: Transformer-coupled sampling accurately captures the effect of backbone helicity on the rotamer state of Phe47. As the degree of helicity increases, the mode centered at  $\pi$  becomes more populated, while the mode centered at  $-\frac{\pi}{3}$  becomes less populated. In the insets, representative configurations are plotted, with the left two plots consisting of samples from the mode centered at  $-\frac{\pi}{3}$ , with the right two plots consisting of samples from the mode centered at  $\pi$ .

uncoupled sampling can often generate configurations with non-bonded distances that are unphysical. With transformer-coupled sampling, we minimize the generation of these distances and generate configurations with distances that are near-commensurate with those observed in an MD simulation.

Second, we consider pairs of side chain atoms that engage in hydrogen bonding. There are three persistent side-chain-side-chain hydrogen bonds in Chignolin, which occur between various atoms in Thr7, Thr9, and Asp4. We plot the distributions of these distances in Figure 4. We observe that the transformer-coupled sampling does not generate configurations with hydrogen bonding comparable to the hydrogen bonding present in the MD dataset. This likely results from our dataset curation strategy, where the training dataset does not consist of Boltzmann-distributed configurations but rather only those that are below some energy threshold. This is also supported in Figure 4, where we also plot the distribution of distances of low energy configurations from relaxed uncoupled sampling. Ultimately, this highlights the limitation of using a purely “bottom-up” strategy to generate a training dataset, which fails to appropriately weigh relevant phenomena like hydrogen bonding. We provide strategies for carrying out reweighting to recapitulate physically important phenomena like hydrogen bonding in Sec. 5.

## 4.2 Intrinsically Disordered Region of the Androgen Receptor (AR-IDR)

Intrinsically disordered proteins (IDPs) are a class of proteins that adopt an ensemble of heterogeneous configurations, with transient local secondary structure propensity [52, 53]. Gaining mechanistic insight into IDP function has tremendous scientific value due to role of these proteins in an enormous array of biological processes and phenomena including transcriptional regulation [54], cellular signal transduction [55, 53], and membraneless organelles [56, 57]. Characterizing the conformational ensemble with atomistic detail constitutes an important first step to piecing apart the structure-ensemble-function relationship for IDPs, though this is not feasible experimentally with NMR or SAXS [58] or computational techniques AlphaFold—[59, 60] which ultimately provides only a small number of structures of questionable thermodynamic relevance. All-atom and coarse-grained simulations offer a promising route towards high-resolution characterization of the structural ensemble, and in light of this promise, extensive effort has been dedicated to developing atomistic [61] and coarse-grained force fields [62, 63, 64].

Coarse-grained simulations paired with backmapping can provide detailed insight into the structural ensemble in a computationally tractable fashion. However, carrying out backmapping from coarse-grained trajectories of IDPs is an especially challenging task as a robust strategy for backmapping will have to contend with sampling rotameric states across a diversity of backbone structures. Here, we investigate our ability to sample rotameric states for an intrinsically disordered region of the androgen receptor (AR) [65, 54]. AR is a transcription factor that contains folded DNA and ligand-binding domains and an intrinsically disordered N-terminal transactivation domain (NTD) [66, 67]. Recent work by Zhu et al. investigated a particular 56 residue region of the NTD, which is bound by two small-molecule inhibitors; using all-atom simulations,

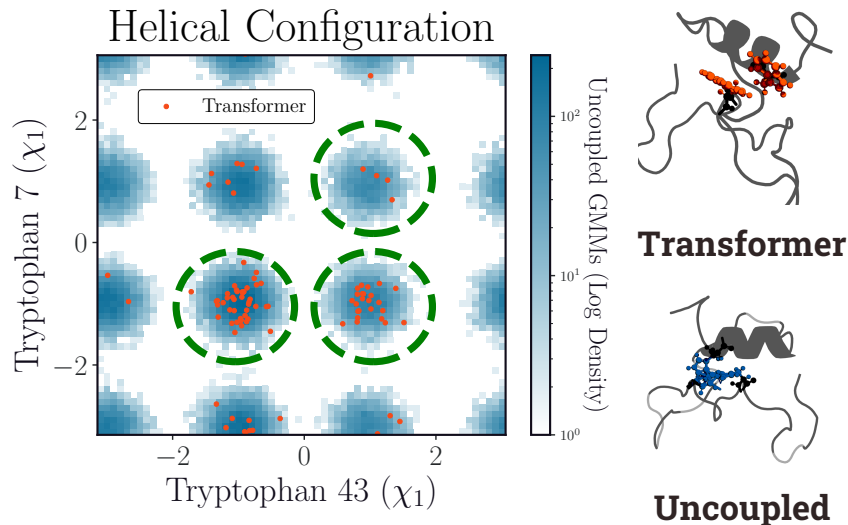


Figure 6: Transformer-coupled sampling accurately captures sequentially long-range correlations between Trp7 and Trp43 for a representative helical molten-globule state. The three modes centered at  $(-\frac{\pi}{3}, -\frac{\pi}{3})$ ,  $(\frac{\pi}{3}, -\frac{\pi}{3})$ , and  $(\frac{\pi}{3}, \frac{\pi}{3})$  correspond to the lowest energy metastable rotamer states and transformer-coupled sampling generally restricts sampling to these modes.

they observed that these inhibitors induce increased helicity in the disordered region, restricting transcription activation [54]. Here, we investigate our ability to carry out backmapping of this intrinsically disordered region, and for notational simplicity, we henceforth term this region AR-IDR.

As in Section 4.1, we assume that we have access to a collection of coarse-grained configurations, which we generate by coarse-graining atomistic configurations from a long all-atom MD simulation [54]. AR-IDR has 51 unique tripeptides, and we similarly carry out long MD simulations for each of these tripeptides in explicit solvent and train corresponding rotamer generators. With AR-IDR, we had access to 57144 backbone configurations, and for each of these configurations, we generated 50000 possible rotamer states by independently sampling all rotamer generators, carried out a short relaxation step, and selected structures with energies below a threshold (see Appendix C). Using again an 80/10/10 train/validation/test-set split, we select the best-performing network on the validation set, and carry out all analyses below on the test set.

### Backbone helicity informs rotameric sampling

In the apo state, the AR-IDR can adopt local helical structures (see Figure 1 and Figure 5 inset), and the degree of helicity influences the allowed rotamer states. Furthermore, two small-molecule inhibitors that target AR-NTD interact with various aromatic residues (Trp7, Trp43, Phe47) [54] that are present in regions that have high helical propensity. As a first test, we examined whether our backmapping strategy could capture the rotamer density of these residues across differing degrees of helicity.

In Figure 5, we consider the effect of helicity on Phe47. Using an order parameter that measures discrepancies from an ideal helix, we categorize the backbone region adjacent to Phe47 into four categories: no helicity, weak helicity, moderate helicity, and strong helicity. We then investigate the effect of this backbone structure on the  $\chi_1$  dihedral angle of Phe47 and compare it to the rotameric states observed during MD simulation. We find that under transformer-coupled sampling, as the degree of helicity increases, there is increased occupancy of the rotamer state centered at  $-\pi$  and decreased occupancy of the rotamer state centered at  $-\frac{\pi}{3}$ . Remarkably, this is a trend that we also observe from atomistic MD simulations, demonstrating that we can capture this effect without access to an existing dataset of rotameric states for this protein. We analyze the consequence of helicity for Trp7 and Trp43 in Figure 10.

## Correlated backmapping of aromatic side chains

Next, we look at a helical “molten-globule”-like state, representative of the structure that AR-IDR maintains when bound by a small-molecule inhibitor. This more compact nature of the protein is a more difficult setting to carry backmapping in due to the close spatial proximity of many residues distant in the primary sequence. In Figure 4.2, we consider a backbone conformation where Trp7 and Trp43 are spatially close, requiring a transformer-based sampling scheme to couple sampling of the respective rotamer states.

For this backbone state, the three modes centered at  $(-\frac{\pi}{3}, -\frac{\pi}{3})$ ,  $(\frac{\pi}{3}, -\frac{\pi}{3})$ , and  $(\frac{\pi}{3}, \frac{\pi}{3})$  correspond to the lowest energy metastable rotamer states, while the modes centered at  $(-\frac{\pi}{3}, \pi)$ ,  $(\frac{\pi}{3}, \pi)$ , and  $(\pi, \pi)$ , would result in rotamer states with unphysical steric overlaps. Finally, the remaining three modes are less favorable statistically but do not generally correspond to rotamer states with steric overlaps. From Figure 4.2, it is clear that transformer-informed sampling directs sampling towards statistically favorable modes (outlined in green), while restricting sampling from statistically unfavorable and unlikely modes. Finally, we note that the imperfections in sampling can be corrected with a reweighting scheme. While this is not outright possible with the transformer-informed sampling, we outline strategies for reweighting in Section 5.

## 5 Outlook

Generative models offer tremendous promise for rapidly sampling large biomolecular systems; however, relying on such a strategy is only viable if we can deploy generative models in settings with task-limited data. In this paper, we outline an approach to sample the rotameric density of proteins via a modular backmapping approach. Crucially, this approach requires no data from the target density *a priori*, and instead, we leverage cheap-to-acquire data from related systems, namely tripeptide simulations, to carry out backmapping.

While this data-free, transformer-based sampling scheme is promising, one of the drawbacks, as discussed earlier, is our inability to reweight samples and provide guarantees that the sampling is Boltzmann distributed. To carry out reweighting, we require the exact likelihood of a generated sample, and computing the likelihood of a transformer-generated sample is not tractable computationally. Normalizing flows are a class of generative models with bespoke architectures designed to enable exact likelihood computation, that, like many neural networks, perform remarkably well in the large-data limit. One feasible approach to carry out reweighting would be to generate large amounts of data using the transformer, and with this data, train a normalizing flow to carry out backmapping. Because the transformer generates samples that have reasonable likelihood under the Boltzmann distribution, reweighting will be more successful than a normalizing flow directly trained on samples from uncoupled rotamer generators. This strategy would also provide a greater diversity of configurations than atomistic MD and would not be susceptible to mode collapse [36].

Integrating a diverse set of data streams will be essential if we are to build scalable generative models that accurately reflect the thermal fluctuations of complex biomolecules. While the approach we outline in this work is “bottom-up” in the sense that physics-based simulations of tripeptides provide models that are then adapted to specific systems, we also foresee employing a “top-down” approach in which the rotamer transformer is also trained on experimental structures. The limitations we see in our present model we believe arise primarily from insufficient data, which a top-down approach will help alleviate. We expect that integrating this data will help capture a diversity of correlations among side chains in many distinct structural motifs.

## Acknowledgements

The authors thank Aaron Dinner and David Wales for the suggestion of using rotamer libraries. The authors would also like to acknowledge Frank Hu for helpful discussions about transformers. This material is based upon work supported by the U.S. Department of Energy, Office of Science, Office of Basic Energy Sciences, under Award Number DE-SC0022917.

**Data and Code Availability:** The data that support the findings of this study are available from the corresponding author upon reasonable request. Our code is available on GitHub at the following url:

<https://github.com/rotskoff-group/transformer-backmapping>.

## References

- [1] Frank Noé, Simon Olsson, Jonas Köhler, and Hao Wu. Boltzmann generators: Sampling equilibrium states of many-body systems with deep learning. *Science*, 365(6457):eaaw1147, September 2019.
- [2] Shriram Chennakesavalu, David J. Toomer, and Grant M. Rotskoff. Ensuring thermodynamic consistency with invertible coarse-graining. *The Journal of Chemical Physics*, 158(12):124126, March 2023. Publisher: American Institute of Physics.
- [3] Shuxin Zheng, Jiyan He, Chang Liu, Yu Shi, Ziheng Lu, Weitao Feng, Fusong Ju, Jiayi Wang, Jianwei Zhu, Yaosen Min, He Zhang, Shidi Tang, Hongxia Hao, Peiran Jin, Chi Chen, Frank Noé, Haiguang Liu, and Tie-Yan Liu. Towards Predicting Equilibrium Distributions for Molecular Systems with Deep Learning, June 2023. arXiv:2306.05445 [physics, q-bio].
- [4] Frank Noé, Gianni De Fabritiis, and Cecilia Clementi. Machine learning for protein folding and dynamics. *arXiv:1911.09811 [physics, q-bio, stat]*, November 2019. arXiv: 1911.09811.
- [5] Tony Lelièvre, Mathias Rousset, and Gabriel Stoltz. *Free Energy Computations: A Mathematical Perspective*. IMPERIAL COLLEGE PRESS, June 2010.
- [6] Kresten Lindorff-Larsen, Stefano Piana, Ron O. Dror, and David E. Shaw. How Fast-Folding Proteins Fold. *Science*, 334(6055):517–520, October 2011. Publisher: American Association for the Advancement of Science.
- [7] Yang Song, Jascha Sohl-Dickstein, Diederik P. Kingma, Abhishek Kumar, Stefano Ermon, and Ben Poole. Score-Based Generative Modeling through Stochastic Differential Equations. February 2022.
- [8] Michael S. Albergo and Eric Vanden-Eijnden. Building Normalizing Flows with Stochastic Interpolants, October 2022. arXiv:2209.15571 [cs, stat].
- [9] Yaron Lipman, Ricky T. Q. Chen, Heli Ben-Hamu, Maximilian Nickel, and Matthew Le. Flow Matching for Generative Modeling. September 2022.
- [10] Federica Gerace, Luca Saglietti, Stefano Saraio Mannelli, Andrew Saxe, and Lenka Zdeborová. Probing transfer learning with a model of synthetic correlated datasets. *Machine Learning: Science and Technology*, 3(1):015030, February 2022. Publisher: IOP Publishing.
- [11] Steve Hanneke and Samory Kpotufe. On the Value of Target Data in Transfer Learning. In *Advances in Neural Information Processing Systems*, volume 32. Curran Associates, Inc., 2019.
- [12] Chieh-Hsin Lai, Yuhta Takida, Naoki Murata, Toshimitsu Uesaka, Yuki Mitsufuji, and Stefano Ermon. FP-Diffusion: Improving Score-based Diffusion Models by Enforcing the Underlying Score Fokker-Planck Equation. In *Proceedings of the 40th International Conference on Machine Learning*, pages 18365–18398. PMLR, July 2023. ISSN: 2640-3498.
- [13] Thomas N. Kipf and Max Welling. Semi-supervised classification with graph convolutional networks. In *5th international conference on learning representations, ICLR 2017, toulon, france, april 24-26, 2017, conference track proceedings*. OpenReview.net, 2017. tex.bibsource: dblp computer science bibliography, <https://dblp.org> tex.biburl: <https://dblp.org/rec/conf/iclr/KipfW17.bib> tex.timestamp: Thu, 25 Jul 2019 14:25:55 +0200.
- [14] Esteban G. Tabak and Eric Vanden-Eijnden. Density estimation by dual ascent of the log-likelihood. *Communications in Mathematical Sciences*, 8(1):217–233, 2010.
- [15] Danilo Rezende and Shakir Mohamed. Variational Inference with Normalizing Flows. In *International Conference on Machine Learning*, pages 1530–1538. PMLR, June 2015. ISSN: 1938-7228.

- [16] Marylou Gabri e, Grant M. Rotskoff, and Eric Vanden-Eijnden. Efficient Bayesian Sampling Using Normalizing Flows to Assist Markov Chain Monte Carlo Methods. In *ICML Workshop on Invertible Neural Networks, Normalizing Flows, and Explicit Likelihood Models*, 2021.
- [17] Laurent Dinh, Jascha Sohl-Dickstein, and Samy Bengio. Density Estimation Using Real NVP. page 32, 2017.
- [18] Conor Durkan, Artur Bekasov, Iain Murray, and George Papamakarios. Neural Spline Flows. In H. Wallach, H. Larochelle, A. Beygelzimer, F. d’Alch e-Buc, E. Fox, and R. Garnett, editors, *Advances in Neural Information Processing Systems*, volume 32. Curran Associates, Inc., 2019.
- [19] R. Chandrasekaran and G. N. Ramachandran. Studies on the Conformation of Amino Acids. *International Journal of Protein Research*, 2(1-4):223–233, 1970. \_eprint: <https://onlinelibrary.wiley.com/doi/pdf/10.1111/j.1399-3011.1970.tb01679.x>.
- [20] Michael J. Bower, Fred E. Cohen, and Roland L. Dunbrack. Prediction of protein side-chain rotamers from a backbone-dependent rotamer library: a new homology modeling tool<sup>11</sup>Edited by B. Honig. *Journal of Molecular Biology*, 267(5):1268–1282, April 1997.
- [21] Roland L. Dunbrack Jr. and Fred E. Cohen. Bayesian statistical analysis of protein side-chain rotamer preferences. *Protein Science*, 6(8):1661–1681, 1997. \_eprint: <https://onlinelibrary.wiley.com/doi/pdf/10.1002/pro.5560060807>.
- [22] Cyrus Levinthal. Are there pathways for protein folding? *Journal de Chimie Physique*, 65:44–45, 1968. Publisher: EDP Sciences.
- [23] Kateri H. DuBay and Phillip L. Geissler. Calculation of Proteins’ Total Side-Chain Torsional Entropy and Its Influence on Protein–Ligand Interactions. *Journal of Molecular Biology*, 391(2):484–497, August 2009.
- [24] Kateri H. DuBay, Gregory R. Bowman, and Phillip L. Geissler. Fluctuations within Folded Proteins: Implications for Thermodynamic and Allosteric Regulation. *Accounts of Chemical Research*, 48(4):1098–1105, April 2015.
- [25] Kateri H. DuBay, Jacques P. Bothma, and Phillip L. Geissler. Long-Range Intra-Protein Communication Can Be Transmitted by Correlated Side-Chain Fluctuations Alone. *PLoS Computational Biology*, 7(9):e1002168, September 2011.
- [26] Roland L Dunbrack. Rotamer Libraries in the 21st Century. *Current Opinion in Structural Biology*, 12(4):431–440, August 2002.
- [27] L. Dicks and D. J. Wales. Exploiting Sequence-Dependent Rotamer Information in Global Optimization of Proteins. *The Journal of Physical Chemistry B*, 126(42):8381–8390, October 2022. Publisher: American Chemical Society.
- [28] Zhichao Miao, Yang Cao, and Taijiao Jiang. RASP: rapid modeling of protein side chain conformations. *Bioinformatics*, 27(22):3117–3122, November 2011.
- [29] Georgii G. Krivov, Maxim V. Shapovalov, and Roland L. Dunbrack Jr. Improved prediction of protein side-chain conformations with SCWRL4. *Proteins: Structure, Function, and Bioinformatics*, 77(4):778–795, 2009. \_eprint: <https://onlinelibrary.wiley.com/doi/pdf/10.1002/prot.22488>.
- [30] John M. Jumper, Karl F. Freed, and Tobin R. Sosnick. Rapid calculation of side chain packing and free energy with applications to protein molecular dynamics, September 2017. arXiv:1610.07277 [physics, q-bio].
- [31] Marc Stieffenhofer, Michael Wand, and Tristan Bereau. Adversarial reverse mapping of equilibrated condensed-phase molecular structures. *Machine Learning: Science and Technology*, 1(4):045014, December 2020. tex.ids= stieffenhofer\_adversarial\_2020 publisher: IOP Publishing.

- [32] Soojung Yang and Rafael Gómez-Bombarelli. Chemically Transferable Generative Backmapping of Coarse-Grained Proteins, March 2023.
- [33] Michael S. Jones, Kirill Shmilovich, and Andrew L. Ferguson. DiAMoNDBack: Diffusion-Denoising Autoregressive Model for Non-Deterministic Backmapping of C $\alpha$  Protein Traces. *Journal of Chemical Theory and Computation*, 19(21):7908–7923, November 2023. Publisher: American Chemical Society.
- [34] Ashish Vaswani, Noam Shazeer, Niki Parmar, Jakob Uszkoreit, Llion Jones, Aidan N Gomez, Łukasz Kaiser, and Illia Polosukhin. Attention is All you Need. In *Advances in Neural Information Processing Systems*, volume 30. Curran Associates, Inc., 2017.
- [35] Jürgen Walther, Pablo D Dans, Alexandra Balaceanu, Adam Hospital, Genís Bayarri, and Modesto Orozco. A multi-modal coarse grained model of DNA flexibility mappable to the atomistic level. *Nucleic Acids Research*, 48(5):e29, March 2020.
- [36] Marylou Gabrié, Grant M. Rotskoff, and Eric Vanden-Eijnden. Adaptive Monte Carlo augmented with normalizing flows. *Proceedings of the National Academy of Sciences*, 119(10):e2109420119, March 2022.
- [37] Daniel Levy, Matt D. Hoffman, and Jascha Sohl-Dickstein. Generalizing Hamiltonian Monte Carlo with Neural Networks. February 2018.
- [38] Jiaming Song, Shengjia Zhao, and Stefano Ermon. A-nice-mc: Adversarial training for MCMC. In I. Guyon, U. V. Luxburg, S. Bengio, H. Wallach, R. Fergus, S. Vishwanathan, and R. Garnett, editors, *Advances in neural information processing systems*, volume 30. Curran Associates, Inc., 2017.
- [39] J. Charlie Maier and Nicholas E. Jackson. Bypassing backmapping: Coarse-grained electronic property distributions using heteroscedastic Gaussian processes. *The Journal of Chemical Physics*, 157(17):174102, November 2022.
- [40] T. N. Bhat, V. Sasisekharan, and M. Vijayan. An analysis of side-chain conformation in proteins. *International Journal of Peptide and Protein Research*, 13(2):170–184, February 1979.
- [41] Jay W. Ponder and Frederic M. Richards. Tertiary templates for proteins. *Journal of Molecular Biology*, 193(4):775–791, February 1987.
- [42] Pinak Chakrabarti and Debnath Pal. The interrelationships of side-chain and main-chain conformations in proteins. *Progress in Biophysics and Molecular Biology*, 76(1-2):1–102, 2001.
- [43] Paul D. Adams, Pavel V. Afonine, Gábor Bunkóczi, Vincent B. Chen, Ian W. Davis, Nathaniel Echols, Jeffrey J. Headd, Li-Wei Hung, Gary J. Kapral, Ralf W. Grosse-Kunstleve, Airlie J. McCoy, Nigel W. Moriarty, Robert Oeffner, Randy J. Read, David C. Richardson, Jane S. Richardson, Thomas C. Terwilliger, and Peter H. Zwart. PHENIX : A comprehensive Python-based system for macromolecular structure solution. *Acta Crystallographica Section D Biological Crystallography*, 66(2):213–221, February 2010.
- [44] E. Mashiach, D. Schneidman-Duhovny, N. Andrusier, R. Nussinov, and H. J. Wolfson. FireDock: A web server for fast interaction refinement in molecular docking. *Nucleic Acids Research*, 36(Web Server):W229–W232, May 2008.
- [45] Mohammad Moghadasi, Hanieh Mirzaei, Artem Mamonov, Pirooz Vakili, Sandor Vajda, Ioannis Ch. Paschalidis, and Dima Kozakov. The Impact of Side-Chain Packing on Protein Docking Refinement. *Journal of Chemical Information and Modeling*, 55(4):872–881, April 2015.
- [46] Andrew M. Watkins, Richard Bonneau, and Paramjit S. Arora. Side-Chain Conformational Preferences Govern Protein–Protein Interactions. *Journal of the American Chemical Society*, 138(33):10386–10389, August 2016.
- [47] Peter Wirnsberger, George Papamakarios, Borja Ibarz, Sébastien Racanière, Andrew J. Ballard, Alexander Pritzel, and Charles Blundell. Normalizing flows for atomic solids. *arXiv:2111.08696 [cond-mat, physics:physics, stat]*, November 2021. arXiv: 2111.08696.

- [48] G.N. Ramachandran, C. Ramakrishnan, and V. Sasisekharan. Stereochemistry of polypeptide chain configurations. *Journal of Molecular Biology*, 7(1):95–99, July 1963.
- [49] Brooke E. Husic, Nicholas E. Charron, Dominik Lemm, Jiang Wang, Adrià Pérez, Maciej Majewski, Andreas Krämer, Yaoyi Chen, Simon Olsson, Gianni de Fabritiis, Frank Noé, and Cecilia Clementi. Coarse graining molecular dynamics with graph neural networks. *The Journal of Chemical Physics*, 153(19):194101, November 2020. Publisher: American Institute of Physics.
- [50] Shinya Honda, Toshihiko Akiba, Yusuke S. Kato, Yoshito Sawada, Masakazu Sekijima, Miyuki Ishimura, Ayako Ooishi, Hideki Watanabe, Takayuki Odahara, and Kazuaki Harata. Crystal Structure of a Ten-Amino Acid Protein. *Journal of the American Chemical Society*, 130(46):15327–15331, November 2008.
- [51] Keri A. McKiernan, Brooke E. Husic, and Vijay S. Pande. Modeling the mechanism of CLN025 beta-hairpin formation. *The Journal of Chemical Physics*, 147(10):104107, September 2017.
- [52] H. Jane Dyson and Peter E. Wright. Intrinsically unstructured proteins and their functions. *Nature Reviews Molecular Cell Biology*, 6(3):197–208, March 2005.
- [53] Peter E. Wright and H. Jane Dyson. Intrinsically disordered proteins in cellular signalling and regulation. *Nature Reviews Molecular Cell Biology*, 16(1):18–29, January 2015.
- [54] Jiaqi Zhu, Xavier Salvatella, and Paul Robustelli. Small molecules targeting the disordered trans-activation domain of the androgen receptor induce the formation of collapsed helical states. *Nature Communications*, 13(1):6390, October 2022.
- [55] Peter E Wright and H.Jane Dyson. Intrinsically unstructured proteins: Re-assessing the protein structure-function paradigm. *Journal of Molecular Biology*, 293(2):321–331, October 1999.
- [56] Vladimir N. Uversky, Irina M. Kuznetsova, Konstantin K. Turoverov, and Boris Zaslavsky. Intrinsically disordered proteins as crucial constituents of cellular aqueous two phase systems and coacervates. *FEBS Letters*, 589(1):15–22, January 2015.
- [57] Clifford P. Brangwynne, Peter Tompa, and Rohit V. Pappu. Polymer physics of intracellular phase transitions. *Nature Physics*, 11(11):899–904, November 2015.
- [58] Massimiliano Bonomi, Gabriella T. Heller, Carlo Camilloni, and Michele Vendruscolo. Principles of protein structural ensemble determination. *Current Opinion in Structural Biology*, 42:106–116, February 2017.
- [59] John Jumper, Richard Evans, Alexander Pritzel, Tim Green, Michael Figurnov, Olaf Ronneberger, Kathryn Tunyasuvunakool, Russ Bates, Augustin Žídek, Anna Potapenko, Alex Bridgland, Clemens Meyer, Simon A. A. Kohl, Andrew J. Ballard, Andrew Cowie, Bernardino Romera-Paredes, Stanislav Nikolov, Rishub Jain, Jonas Adler, Trevor Back, Stig Petersen, David Reiman, Ellen Clancy, Michal Zielinski, Martin Steinegger, Michalina Pacholska, Tamas Berghammer, Sebastian Bodenstein, David Silver, Oriol Vinyals, Andrew W. Senior, Koray Kavukcuoglu, Pushmeet Kohli, and Demis Hassabis. Highly accurate protein structure prediction with AlphaFold. *Nature*, 596(7873):583–589, August 2021.
- [60] Kiersten M. Ruff and Rohit V. Pappu. AlphaFold and Implications for Intrinsically Disordered Proteins. *Journal of Molecular Biology*, 433(20):167208, October 2021.
- [61] Paul Robustelli, Stefano Piana, and David E. Shaw. Developing a molecular dynamics force field for both folded and disordered protein states. *Proceedings of the National Academy of Sciences*, 115(21), May 2018.
- [62] Andreas Vitalis and Rohit V. Pappu. ABSINTH: A new continuum solvation model for simulations of polypeptides in aqueous solutions. *Journal of Computational Chemistry*, 30(5):673–699, April 2009.
- [63] Andrew P. Latham and Bin Zhang. Maximum Entropy Optimized Force Field for Intrinsically Disordered Proteins. *Journal of Chemical Theory and Computation*, 16(1):773–781, January 2020.

- [64] Andrew P. Latham and Bin Zhang. Unifying coarse-grained force fields for folded and disordered proteins. *Current Opinion in Structural Biology*, 72:63–70, February 2022.
- [65] Eva De Mol, R. Bryn Fenwick, Christopher T. W. Phang, Victor Buzón, Elzbieta Szulc, Alex De La Fuente, Albert Escobedo, Jesús García, Carlos W. Bertoncini, Eva Estébanez-Perpiñá, Iain J. McEwan, Antoni Riera, and Xavier Salvatella. EPI-001, A Compound Active against Castration-Resistant Prostate Cancer, Targets Transactivation Unit 5 of the Androgen Receptor. *ACS Chemical Biology*, 11(9):2499–2505, September 2016.
- [66] James Reid, Sharon M. Kelly, Kate Watt, Nicholas C. Price, and Iain J. McEwan. Conformational Analysis of the Androgen Receptor Amino-terminal Domain Involved in Transactivation. *Journal of Biological Chemistry*, 277(22):20079–20086, May 2002.
- [67] Derek N. Lavery and Iain J. McEwan. Structural Characterization of the Native NH<sub>2</sub>-Terminal Transactivation Domain of the Human Androgen Receptor: A Collapsed Disordered Conformation Underlies Structural Plasticity and Protein-Induced Folding. *Biochemistry*, 47(11):3360–3369, March 2008.
- [68] B. Leimkuhler and C. Matthews. Rational Construction of Stochastic Numerical Methods for Molecular Sampling. *Applied Mathematics Research eXpress*, page abs010, June 2012.
- [69] James A. Maier, Carmenza Martinez, Koushik Kasavajhala, Lauren Wickstrom, Kevin E. Hauser, and Carlos Simmerling. ff14SB: Improving the Accuracy of Protein Side Chain and Backbone Parameters from ff99SB. *Journal of Chemical Theory and Computation*, 11(8):3696–3713, August 2015.
- [70] William L. Jorgensen, Jayaraman Chandrasekhar, Jeffrey D. Madura, Roger W. Impey, and Michael L. Klein. Comparison of simple potential functions for simulating liquid water. *The Journal of Chemical Physics*, 79(2):926–935, July 1983.
- [71] F. Pedregosa, G. Varoquaux, A. Gramfort, V. Michel, B. Thirion, O. Grisel, M. Blondel, P. Prettenhofer, R. Weiss, V. Dubourg, J. Vanderplas, A. Passos, D. Cournapeau, M. Brucher, M. Perrot, and E. Duchesnay. Scikit-learn: Machine Learning in Python. *Journal of Machine Learning Research*, 12:2825–2830, 2011.

## A Rotamer Library

### A.1 Tripeptide simulations

We ran MD simulations of tripeptides in explicit solvent to exhaustively sample the rotameric density. Each simulation was conducted in the NVT ensemble using the under-damped BAOAB integrator [68] with a time step of 0.001 ps and a friction coefficient of  $\gamma = 0.1 \text{ ps}^{-1}$ . We did not incorporate any bond constraints. While treating bonds as constraints allows a larger integration time step, flexible bonds better capture the fluctuations of the tripeptide, which is desirable for reweighting. We ran each tripeptide simulation for 48 GPU hours at 300K, resulting in trajectories that ranged from 0.5-1  $\mu\text{s}$ .

For simplicity, we only ran simulations for tripeptides that were relevant to Chignolin and AR-IDR. For each non-terminal residue  $\text{res}_i$  in the protein, we ran a corresponding simulation for the tripeptide  $\text{res}_{i-1}\text{res}_i\text{res}_{i+1}$ , where we used information from the central residue for training the rotamer generator for residue  $i$ . For the first residue  $\text{res}_1$  the corresponding tripeptide simulation was  $\text{res}_i\text{res}_{i+1}\text{res}_{i+1}$  where we used information from the first residue of the tripeptide for training the rotamer generator. For the last residue  $\text{res}_m$ , the corresponding tripeptide was  $\text{res}_{m-2}\text{res}_{m-1}\text{res}_m$ , where we used information from the last residue of the tripeptide for training the rotamer generators.

For Chignolin, there were 8 unique tripeptides and for AR-IDR, there were 51 unique tripeptides. For the Chignolin tripeptides we used the Amber ff14SB force field [69] with the TIP3P water model [70]. For the AR-IDR tripeptides, we used the a99SB-disp force field and a99SB-disp water model [61].

### A.2 Reconstructing a side chain

We use an internal coordinate representation based on bond distances, bond angles, and dihedral angles to carry out side chain reconstruction. This representation is often collated in a “ $z$ -matrix,” where a sample  $z$ -matrix is, for example,

$$\begin{bmatrix} \text{atom}_1 & \text{atom}_2 & \text{atom}_3 & \text{atom}_4 \\ \text{atom}_2 & \text{atom}_3 & \text{atom}_4 & \text{atom}_5 \\ \text{atom}_3 & \text{atom}_4 & \text{atom}_5 & \text{atom}_6 \end{bmatrix}. \quad (3)$$

Given the Cartesian coordinates of  $\text{atom}_1$ ,  $\text{atom}_2$ , and  $\text{atom}_3$ , the bond length between  $\text{atom}_3$  and  $\text{atom}_4$ , the bond angle between  $\text{atom}_2, \text{atom}_3$ , and  $\text{atom}_4$ , and the dihedral angle between  $\text{atom}_1, \text{atom}_2, \text{atom}_3$ , and  $\text{atom}_4$ , it is straightforward to compute the Cartesian coordinate of  $\text{atom}_4$  using elementary linear algebra.

The appropriate coordinates, bond lengths, bond angles, and dihedrals can then be used to iteratively determine the coordinates of  $\text{atom}_5$ , and  $\text{atom}_6$ . For every residue considered in our investigation, we have defined a corresponding  $z$ -matrix, where the dihedral angle defined by the  $i$ th row corresponds to the dihedral angle  $\chi_i$ . We refer the reader to our code for the definitions of a  $z$ -matrix for a particular residue.

From the tripeptide simulations (see Appendix A.1), we recorded the appropriate bond lengths, bond angles, and dihedral angles for every row in our  $z$ -matrix, which we then used to train our rotamer generators.

### A.3 Gaussian Mixture Models

We use a Gaussian Mixture Model (GMM) as a generator for the internal coordinates for a given residue. In this representation, the distribution of  $z$ -matrix coordinates is approximated as,

$$\rho^{\text{GMM}} = \sum_{i=1}^K \phi_i \mathcal{N}(\mu_i, \Sigma_i). \quad (4)$$

Making the standard assumption that dihedral angles are uncorrelated from bond lengths and bond angles, for a residue with  $z$ -matrix  $Z \in \mathbb{R}^{k \times 4}$ , we train a Gaussian Mixture Model (GMM) to generate bond lengths and bond angles and a second Gaussian Mixture Model (GMM) to generate dihedral angles. During reconstruction, we concurrently draw samples from the coupled bond length and bond angle generator  $\rho^{\text{GMM}_{l,a}}$  and the dihedral generator  $\rho^{\text{GMM}_d}$ . Given that the joint distribution of bond lengths and bond angles is unimodal, for  $\rho^{\text{GMM}_{l,a}}$ , the number of components  $K = 1$ , and  $\mu_i \in \mathbb{R}^{2k}$  and  $\Sigma_i \in \mathbb{R}^{2k \times 2k}$ . For  $\rho^{\text{GMM}_d}$ , the number of components is defined on a per-residue basis and was manually identified (Table 1).

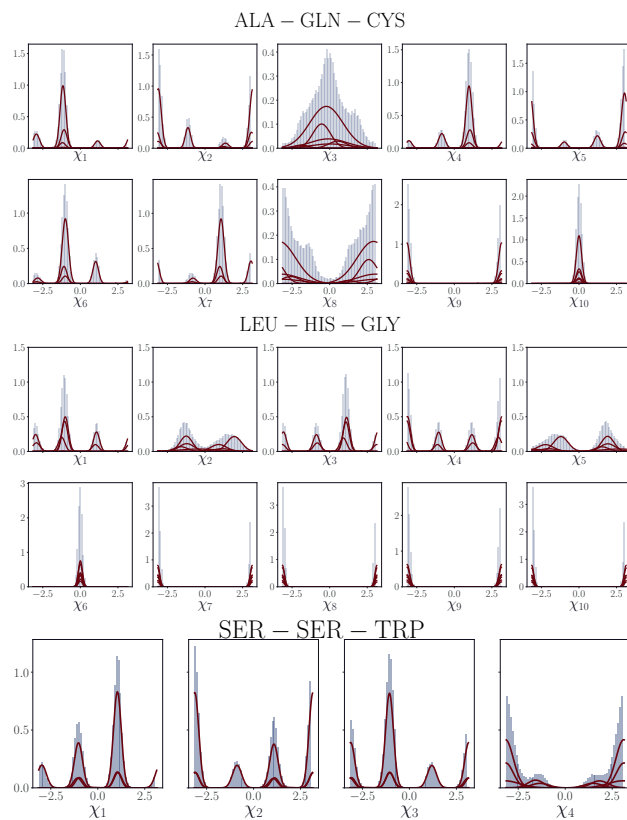


Figure 7: Distribution of  $\chi$  dihedrals for select AR-IDR triptptide simulations. Components Gaussians are overlaid in maroon and are scaled by their mixture weight  $\phi_i$ . Most modes are Gaussian-like but certain modes (e.g.  $\chi_8$  of GLN) are less Gaussian-like.

Number of Gaussian Components	
Residue Name	K
ACE	3
NME	3
ALA	3
ARG	48
ASN	16
ASP	64
CYS	8
GLN	14
GLU	64
GLY	N/A
HIS	8
LEU	64
LYS	96
MET	64
PHE	8
PRO	2
SER	12
THR	32
TRP	8
TYR	16
VAL	32

Table 1: Number of Gaussian components used for side chain dihedral generator. Residues not included here were not present in proteins investigated in this work.

The GMMs are trained using a standard Expectation-Maximization (EM) algorithm using the `scikit-learn` package [71]. This optimization process is computationally efficient, with the largest residues taking less than ten CPU minutes. Importantly, we can interpret each Gaussian component of  $\rho^{\text{GMM}_d}$  as corresponding to a particular rotameric state, with  $\mu_i$  defined as the mean dihedral coordinate of that state,  $\Sigma_i$ , the covariance matrix of that state and  $\phi_i$ , the relative proportion of that rotamer state relative to other rotamer states. We include the distributions of select dihedral angles and their components in Figure 7.

## B Computational details for transformer

We use the implementation of the transformer model [34] available in `PyTorch`. Our approach for the transformer architecture and training is similar to general implementations, with a few small differences, which we note below. The transformer relies on an encoder-decoder framework, where an input backbone sequence is encoded to autoregressively decode an output rotamer sequence. We consider the sequence of backbone dihedrals and residue identities as our input sequence and the sequence of components of the GMM (see Section A.3) to be the output sequence. See Table 2 for relevant hyperparameters.

### B.1 Backbone encoder

We represent the backbone using a sequence of categorical and continuous features corresponding to each residue. Each residue has a single categorical feature corresponding to its amino acid identity, which is passed into an `Embedding` layer. Because the two systems we investigate here do not individually contain all 20 amino acids, in our `Embedding` lookup table, we only include amino acids that are present in the protein. The  $\phi$  and  $\psi$  dihedral angles contain rich information about the backbone and furthermore are strongly correlated with  $\chi_1$ , the dihedral angle associated with the  $\gamma$ -Carbon (for appropriate residues). With that in mind, we consider a continuous tokenization that employs the  $\phi$  and  $\psi$  angles. To avoid issues with the

Hyperparameters		
Hyperparameter	Chignolin	AR-IDR
Number of Encoder Layers	6	6
Number of Decoder Layers	6	6
Number of Attention Heads	8	8
Number of Encoder Tokens ( $n_{\text{tokens}}^{\text{bb}}$ )	7	15
Number of Decoder Tokens ( $n_{\text{tokens}}^{\text{rot}}$ )	67	67
Embedding Dimension ( $e_{\text{dim}}$ )	256	256
Optimizer	Adam	Adam
Learning Rate	$1 \times 10^{-6}$	$1 \times 10^{-6}$
Number of Datapoints	62M	4M
Batch Size	512	512

Table 2: Relevant hyperparameters for transformer training

periodicity of dihedral angles (e.g.  $\pi$  and  $-\pi$  are equivalent), we use the following continuous tokenization:

$$\begin{bmatrix} \sin(\phi_1) & \sin(\phi_2) & \cdots & \sin(\phi_m) \\ \cos(\phi_1) & \cos(\phi_2) & \cdots & \cos(\phi_m) \\ \sin(\psi_1) & \sin(\psi_2) & \cdots & \sin(\psi_m) \\ \cos(\psi_1) & \cos(\psi_2) & \cdots & \cos(\psi_m) \end{bmatrix}, \quad (5)$$

where  $m$  denotes the protein sequence length. Given a sequence of length  $m$  and an embedding dimension of size  $e_{\text{dim}}$ , the sequence of categorical features is embedded—via the **Embedding** lookup table—according to a transformation  $\mathbb{N}^m \rightarrow \mathbb{R}^{m \times e_{\text{dim}}/2}$ , while the sequence of continuous features is embedded according to a standard **Linear** layer  $\mathbb{R}^{m \times 4} \rightarrow \mathbb{R}^{m \times e_{\text{dim}}/2}$ . Finally, the categorical and continuous embeddings are concatenated to produce an embedding of size  $\mathbb{R}^{m \times e_{\text{dim}}}$ , which is then passed through a standard sinusoidal positional encoder [34] and into the encoder block of the transformer. We refer the reader to our code for additional details.

## B.2 Rotamer decoder

Using the input sequence of backbone features, we aim to decode a rotamer sequence consisting of Gaussian component indices that can subsequently be used to generate rotamer states. This rotamer sequence can be defined as  $(C_1, C_2 \dots C_m)$  where  $C_j \in [1, K_{\text{max}}]$  denotes the index of the Gaussian component for  $\rho_j^{\text{GMM}}$  (i.e. the dihedral GMM of the  $j$ th residue) and  $K_{\text{max}} = \max(K_1, K_2, \dots K_n)$  corresponds to the max number of total components across all dihedral GMMs. This last point is an important one; for residue  $j$ , we do not constrain the component index to be less than  $K_j$  but instead constrain it to be less than  $K_{\text{max}}$ . While this results in a weaker inductive bias, it allows for a much simpler architecture and training process. Finally, we prepend a start-of-sequence token and append an end-of-sequence token to the sequence (SOS,  $C_1, C_2 \dots C_m$ , EOS).

Denoting the entire input backbone sequence  $\mathbf{x}$ —where  $\mathbf{x}$  consists of both categorical and continuous features—and the rotamer sequence as  $\mathbf{y}$ , we can train the transformer according to the following cross-entropy loss

$$\mathcal{L}(\theta) = - \sum_{j=1}^{m+1} \text{CE}(\mathbf{y}_{j+1}, f(\mathbf{x}, \mathbf{y}_{1:j}; \theta)), \quad (6)$$

where CE is the cross-entropy loss,  $f$  is the transformer, and  $\theta$  is the parameters of the transformer neural network. In practice, the computation of this loss can be parallelized across the sequence by applying an appropriate masking operation. We refer the reader to our code for further implementation details.

---

**Algorithm 1** Generating a sequence of components

---

- 1: Initialize transformer  $f$  and load trained parameters  $\theta$
  - 2: Prepare backbone encoder sequence  $\mathbf{x}$
  - 3: Defined  $y_{\text{next}} = \text{SOS}$
  - 4: Define  $\mathbf{y} = []$
  - 5: Append  $y_{\text{next}}$  to  $\mathbf{y}$
  - 6: **while**  $y_{\text{next}} \neq \text{EOS}$  **do**
  - 7:      $y_{\text{pred}} = f(\mathbf{x}, \mathbf{y}; \theta)$
  - 8:     Sample  $y_{\text{next}}$  from  $y_{\text{pred}}$
  - 9:     Append  $y_{\text{next}}$  to  $\mathbf{y}$
- 

### B.3 Predicting a sequence of components

During inference time, conditioned on a backbone structure, we seek to generate a sequence of rotamer components that can be subsequently used to sample rotamers across the full protein. Denoting the sequence of backbone features  $\mathbf{x}$  (see Appendix B.1, B.2 for further details), our initial rotamer sequence  $\mathbf{y}_{1:1} = (\text{SOS})$ , where SOS represents the start-of-sequence token. As in Appendix B.2, the backbone sequence is passed into the encoder block of the transformer and the rotamer sequence is passed into the decoder block of the transformer. The output of the transformer  $f(\mathbf{x}, \mathbf{y}_{1:j}; \theta) \in \mathbb{R}^{n_{\text{tokens}}^{\text{rot}}}$  is a multinomial distribution, where  $P(C_j = k) = f(\mathbf{x}, \mathbf{y}_{1:j}; \theta)_k$ . While many strategies exist for autoregressively generating a sequence, here, we select a straightforward strategy; for every element in the sequence, we randomly sample  $C_j$  according to the multinomial distribution generated by the transformer  $f(\mathbf{x}, \mathbf{y}_{1:j}; \theta) \in \mathbb{R}^{n_{\text{tokens}}^{\text{rot}}}$ . This process occurs until an end-of-sequence token is sampled, at which point the sequence terminates. See Algorithm 1 for a summary of the sequence generation process.

The number of components is residue-specific; smaller residues generally have a smaller number of components, while larger residues (e.g. those with longer alkyl chains) contain a larger number of components. The number of tokens for the decoder  $n_{\text{tokens}}^{\text{rot}}$  is fixed and corresponds to the maximum number of components across all dihedral GMMs. During inference, if, for any single sequence  $j$ , a sampled  $C_j > K_j$ , where  $K_j$  is the number of components for the dihedral GMM of the  $j$ th residue, the sequence is considered invalid. For Glycine, we do not need to backmap any atoms but still include it in our sequence and so assign it a separate token. As a result, including the special Glycine token, the SOS token, and the EOS token,  $n_{\text{tokens}}^{\text{rot}} = C_{\text{max}} + 3$

Furthermore, in many tasks transformers are deployed to generate sequences of variable lengths. In the task we consider here, we are interested in generating sequences of a fixed length as the number of residues for the proteins we consider is fixed. As noted, we grow a sequence autoregressively until the end-of-sequence (EOS) token is reached. If the length of the generated sequence (including the SOS and EOS token) is not  $m + 2$ , the sequence is considered invalid. We plot the proportion of valid generated sequences across all backbones in the test in Figure 8. The sequence validity is high across all backbones demonstrating our model can capture the underlying structure of the rotamer sequence.

## C Details for Chignolin and AR-IDR

To train the transformer according to Eq. 6, we of course need access to a dataset. The setting we consider here is one in which we have access to a collection of backbone configurations, which can be obtained by coarse-grained simulations. Here, we select structures from all-atom MD simulations and coarse-grain these structures to a backbone resolution. We backmap each of these backbone structures by sampling from the residue-specific GMMs  $\rho_j^{\text{GMM}_d}$  and  $\rho_j^{\text{GMM}_{l,a}}$ , in an uncoupled fashion. This strategy enables us to rapidly create a large number of independent structures. Of course, this uncoupled sampling strategy will result in many high-energy unphysical configurations. Furthermore, many structures will have a high energy, but a structure that is quantitatively very similar to a low energy structure. Often, a small change in the conformation (0.01 Å) can dramatically reduce the energy of a structure by many  $k_B T$ . With this in mind, we carry out a short relaxation step of all structures. Finally, we select all configurations below  $-50 k_B T$  and use these configurations for our dataset.

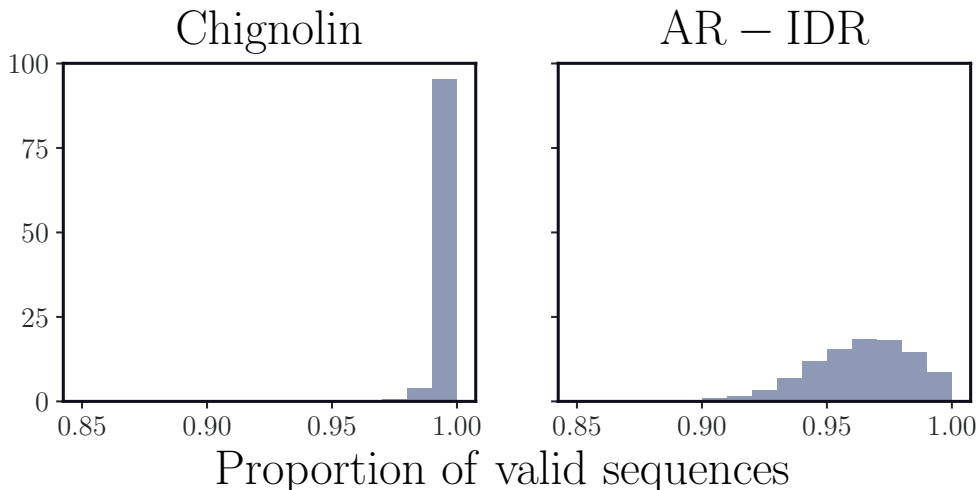


Figure 8: Proportion of valid sequences across all backbones in the test sets of Chignolin and AR-IDR. For a given backbone, the median sequence validity is 1.0 for Chignolin and 0.97 for AR-IDR.

We note again that, while the configurations we select are comparatively low-energy and have statistical validity under the true Boltzmann distribution, our dataset is *not* Boltzmann-distributed. Furthermore, we note that technically we can—under a relaxation scheme that uses a reversible integrator—compute a reweighting factor exactly and ensure our samples are Boltzmann-distributed. However, the entropy of our proposal scheme via uncoupled GMMs is much greater than that of the true rotameric density, and this results in reweighting factors dominated by a handful of terms. Practically under such a reweighting scheme, most of the configurations would get down-weighted, greatly diminishing sample diversity in a reweighted dataset. Because of this limitation, we relax the requirement that our training set be Boltzmann distributed, with the goal of carrying out a reweighting step at a downstream step (see Section 5).

## C.1 Chignolin

For Chignolin, we selected 50000 backbone configurations from a long MD simulation [49]. For each of these backbone configurations, we generated 10000 possible states via uncoupled rotameric sampling, carried out a relaxation step, and selected all configurations below  $-50 k_B T$ , where  $T = 300\text{K}$ . The relaxation step consisted of 5 steps of Verlet integration with  $dt=0.001$  ps at 300K using an implicit solvation model. We used a train/validation/test, where the split was done at the backbone level so that no backbone configuration was present in two or more sets. This led to a training dataset of 62 million configurations, where for each backmapped configuration, we recorded the relevant backbone information and the components of the dihedral GMMs that were used to generate the configuration.

To be consistent with the indexing in the trajectory obtained from [49], the ACE cap is indexed at 1, so TYR2 corresponds to the first non-cap residue, TYR3 the second non-cap residue, and TYR11 the tenth and terminal non-cap residue.

## C.2 AR-IDR

For the intrinsically disordered region of the androgen receptor (AR-IDR), we selected 57144 backbone configurations from a long MD simulation [54]. For each of these backbone configurations, we generated 50000 possible states via uncoupled rotameric sampling, carried out a relaxation step, and selected all configurations below  $-50 k_B T$ , where  $T = 300\text{K}$ . The relaxation step consisted of 20 steps of an overdamped Langevin integration with  $dt=0.00002$  ps and a friction coefficient of  $\gamma = 100.0 \text{ ps}^{-1}$  at 300 K using an implicit solvation model. We used a train/validation/test, where the split was done at the backbone level so that no backbone configuration was present in two or more sets. This led to a training dataset of 4 million

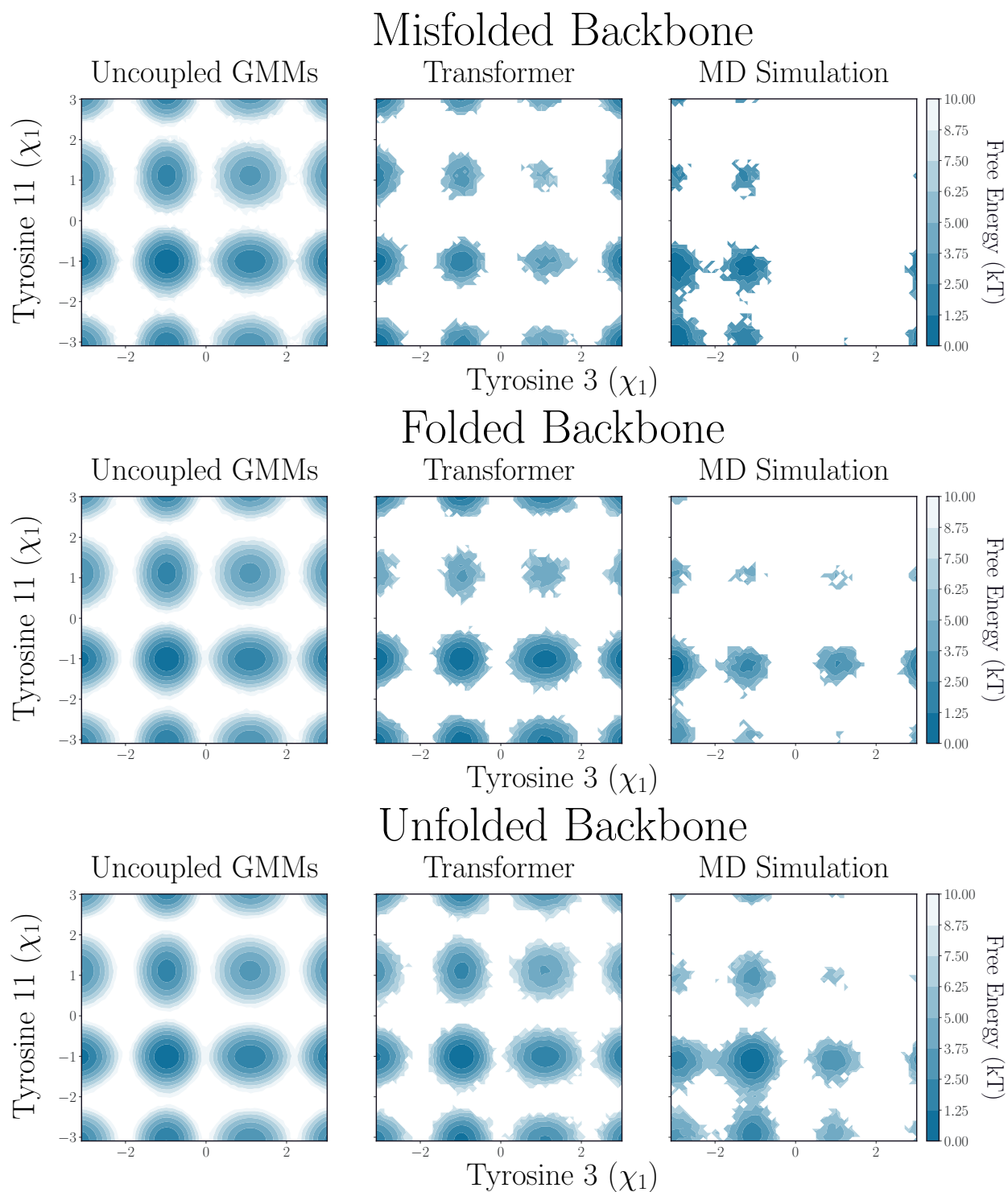


Figure 9: For transformer-coupled sampling and MD simulation, as the hairpin interior becomes more obstructed (unfolded  $\rightarrow$  folded  $\rightarrow$  misfolded), the rotamer entropy decreases, and more states become disallowed. Sampling uncoupled generators does not recapitulate this trend.

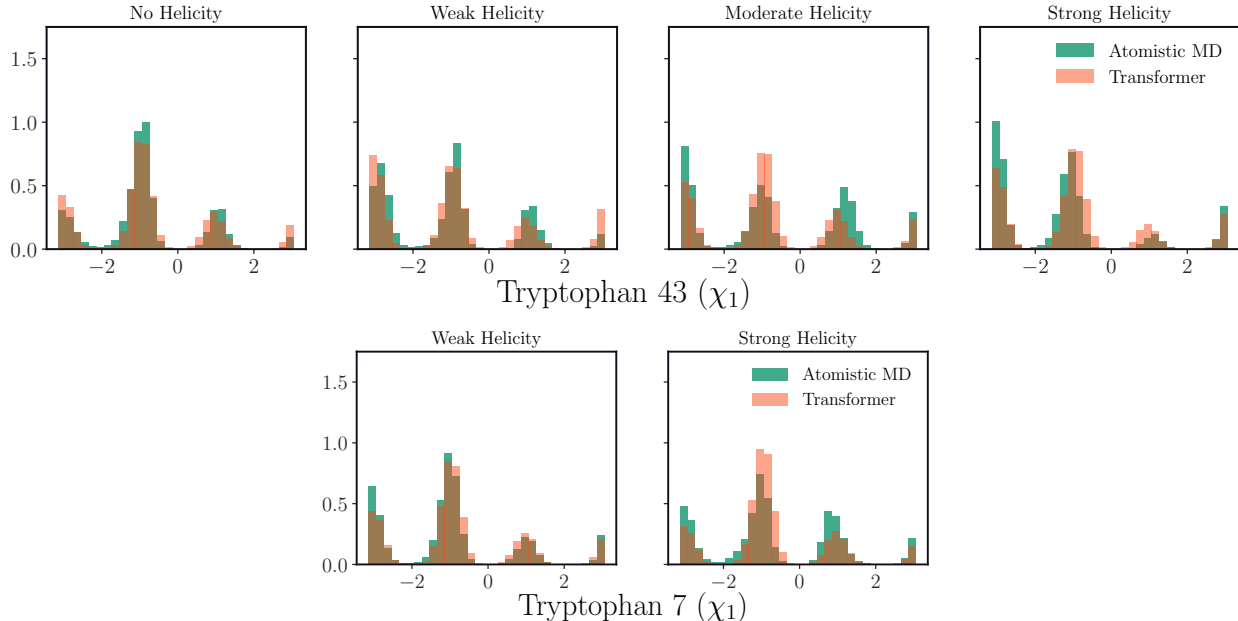


Figure 10: Effect of backbone helicity on rotamer state of Trp43 and Trp7. Transformer-coupled sampling is in strong agreement with rotamer states observed during MD simulation.

configurations, where for each backmapped configuration, we recorded the relevant backbone information and the components of the dihedral GMMs that were used to generate the configuration.

For the AR-IDR, the original trajectory considered a 56 residue region (L391-G446 region) of the N-terminal transactivation domain; for simplicity, we reindex that in our analysis such that the ACE cap is indexed at 0. So, Trp7, Trp43, and Phe47 in our analysis corresponds to Trp397, Trp433, and Phe437 in [54].

To define helicity, we used the order parameter  $S_\alpha$  in [54], which measures discrepancy from an ideal helix using a sliding window of length six residues. For Phe7, we consider the  $S_\alpha$  computed from the four windows starting at residues 3-7. For Phe7, we categorize the backbone as weakly helix ( $S_\alpha < 0.5$ ) and strongly helix ( $S_\alpha \geq 0.5$ ). For Trp43 and Phe47, which reside in the same helix-forming region, we measure the helicity from the five windows starting at residues 38-43. With Phe7, we defined four classes for helicity: no helix ( $S_\alpha < 0.15$ ), weakly helix ( $0.15 \leq S_\alpha < 0.4$ ), moderately helix ( $0.4 \leq S_\alpha < 0.7$ ), and strongly helix ( $S_\alpha \geq 0.7$ ).

Below we analyze the effect of helicity on Trp7 and Trp43. For Trp43 as the degree of helicity increases, the rotamer state centered at  $\pi$  becomes more probable under both the transformer-coupled scheme and the long MD simulation. For Trp7, we observe that the rotamer density is weakly dependent on the degree of helicity in MD simulations and this is a trend that is also recapitulated in transformer-informed sampling.